Design Study of a Dedicated Head and Neck Cancer PET System

Mohan Li, *Student Member, IEEE*, Brett Yockey, and Shiva Abbaszadeh, *Member, IEEE*

***Abstract*—The tumor-involved regions of head and neck cancer (HNC) have complex anatomical structures and vital physiological roles. As a consequence, there is a need for high sensitivity and high spatial resolution dedicated HNC PET scanner. The purpose of this article is to evaluate and optimize system design that includes detecting materials and geometries. For the detecting material, two scanners with the same two-panel geometry based on cadmium zinc telluride (CZT) and lutetium–yttrium oxyorthosilicate (LYSO) were evaluated. For the system geometry, four CZT scanners with two-panel, lengthened two-panel, four-panel, and full-ring geometries were evaluated. A cylinder phantom with sphere lesions and an XCAT phantom in the head and neck region were simulated. The results showed that the sensitivity of the 40-mm thickness CZT system and the 20-mm thickness LYSO system were comparable. However, the multiple interaction photon events recovery accuracy of the CZT system was about 20% higher. The in-panel and orthogonal-panel spatial resolutions of CZT are 0.58 and 0.74 mm, while those of LYSO are 0.70 and 1.40 mm. For system geometry, the four-panel and full-ring scanners have a higher contrast recovery coefficient (CRC) and contrast-to-noise ratio (CNR) than the two-panel and lengthened two-panel scanners. However, a 5-mm lesion in the XCAT phantom was visualized within 6 min in the two-panel system.**

***Index Terms*—Dedicated positron emission tomography (PET), head and neck cancer (HNC), Monte Carlo simulation, system design.**

I. Introduction

HEAD and neck cancer (HNC) accounts for approximately 4% of all cancers in the United States [1] and the overall annual mortality rate is 23% [2]. Whole-body positron emission tomography (PET) and its combination with computed tomography (CT) are commonly used for HNC diagnosis, staging, treatment planning, and assessing response to therapy [3]–[6]. Compared to CT, magnetic resonance imaging, sonographic and histopathological findings, PET imaging shows the highest sensitivity and specificity for detecting lymph node metastases of HNC [7].

Manuscript received September 14, 2019; revised October 23, 2019 and December 30, 2019; accepted January 1, 2020. Date of publication January 3, 2020; date of current version July 2, 2020. This work was supported by in part by NIH under Grant R01-EB028091, and in part by the Cancer Scholars for Translational and Applied Research Program jointly funded by the Carle Foundation Hospital and the University of Illinois. *(Corresponding author: Mohan Li.)*

Mohan Li and Shiva Abbaszadeh are with the Department of Nuclear, Plasma, and Radiological Engineering, University of Illinois at Urbana–Champaign, Urbana, IL 61801 USA (e-mail: mohanli2@illinois.edu).

Brett Yockey is with Carle Foundation Hospital, Urbana, IL 61801 USA.

Color versions of one or more of the figures in this article are available online at http://ieeexplore.ieee.org.

Digital Object Identifier 10.1109/TRPMS.2020.2964293

However, lesions in this region can be challenging to diagnose due to the thin, soft tissues within the neck, which require a high-resolution imaging system. The spatial resolution of the whole-body PET is typically 4–6 mm [8], [9]. For structures less than twice the reconstructed image resolution, the true amount of activity is not completely captured [10]. The poor spatial resolution of the whole-body PET hinders the precise delineation of the primary tumor of HNC and limits the detection of tumor involvement in lymph nodes smaller than 4–5 mm. Besides, it also results in a large number of reported false-negatives in lymph nodes (for example, 80%) [11]–[13]. Researchers [14] from Duke University Medical Center have introduced a dedicated HNC PET acquisition protocol with longer scan time in the HN bed position to improve the detection ability of PET imaging in HNC. The dedicated HN protocol has advantages in detecting lymph nodes smaller than 15 mm compared to the standard protocol. However, in terms of evaluating primary tumors and detecting lymph nodes smaller than 10 mm, there are no significant differences between the standard protocol and the dedicated HN protocol [13], [14].

Due to the complex anatomy and vital physiological role of the tumor-involved structures, the goal of HNC treatment is not only to improve survival outcomes but also to preserve organ functions [15]. An improvement in resolution in a PET image to better define the boundary of tumors is significant for the treatment planning and monitoring of HNC. In supraglottic squamous cell carcinoma, for example, if it involves thyroid cartilage, it is T4 and unresectable. If it does not involve thyroid cartilage, it is T3 and can be cured with surgery. Another example is that if supraglottic squamous cell carcinoma does not cross the anterior commissure, patients can have supraglottic laryngectomy and can be cured without losing voice.

As a result, there is a need for high spatial resolution and high sensitivity PET imaging in HNC. We are designing a high-resolution add-on dedicated HNC PET scanner to complement the whole-body PET scanner. This system will image the patients right after the whole-body PET scanning without injecting any extra dose to the patient. The dedicated system will provide extra information for scenarios when radiologists are looking for small lymph nodes or well-defined tumor boundaries. Fig. 1 shows an illustration of the add-on dedicated system [16], [17].

With more accurate detection of small lymph nodes and estimation of the extent of tumor growth, the dedicated head and neck will provide physicians with more freedom to choose

This work is licensed under a Creative Commons Attribution 4.0 License. For more information, see https://creativecommons.org/licenses/by/4.0/

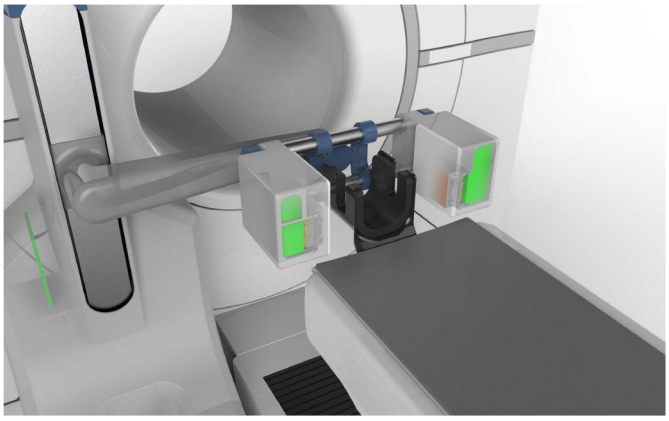

Fig. 1. Illustration of an add-on dedicated HNC PET scanner integrated into the standard whole-body PET/CT imaging workflow. The gantry is implemented to interface with the patient bed to image the patient right after the whole-body PET scanning.

treatment options, including surgery, radiation therapy, and chemotherapy. It helps with more accurate radiation dose planning and will lead to better patient outcomes such as preserving organ functions. It also improves confidence in differentiating post-treatment changes from tumor recurrence.

To design such a dedicated system, the first consideration is the detecting material. Cadmium zinc telluride (CZT) detectors and lutetium–yttrium oxyorthosilicate (LYSO) combined with silicon photomultiplier (SiPM) detectors are investigated for the HNC PET scanner. Compared with LYSO, CZT has a high energy resolution, submillimeter intrinsic spatial resolution [18], [19], and intrinsically achievable depth-of-interaction (DOI) information. It has been used for the small field of view (FOV) and high-resolution PET applications such as small animal imaging [20]–[23]. The high energy resolution and high spatial resolution of CZT detectors are also important for correctly identifying the first interaction position in multiple interaction photon events (MIPEs) using Compton kinematics.

Another important consideration for designing a dedicated PET is the system geometry. Compared with a whole-body PET scanner, dedicated PET often utilizes smaller and compact geometry to adapt to the dedicated imaging environment and improve the system sensitivity [24]. For example, dedicated brain PET has ring and helmet geometries [25]–[28], and dedicated breast PET has two-panel and ring geometries [29]–[32]. In this article, we consider two-panel, lengthened two-panel, four-panel, and full-ring geometries for the sake of high sensitivity and patient's comfort.

The purpose of this article is to evaluate and optimize system design among different detecting materials and geometries. For detecting material, two scanners with the same two-panel geometry based on CZT and LYSO are compared in terms of photon coincidence sensitivity, MIPEs recoverability, noise equivalent count (NEC) rate, and spatial resolution. For system geometry, CZT scanners with two-panel, lengthened two-panel, four-panel, and full-ring geometries are compared in terms of contrast recovery coefficient (CRC) and contrast-to-noise ratio (CNR) of reconstructed images.

II. Methods and Materials

A. Detecting Material

Two systems with the same stationary two-panel geometry based on CZT and LYSO were built in GATE [33]. Based on the human head size [34], the panel was set as 150×200 mm^2, and the distance between the two panels was 200 mm. For the LYSO system, the LYSO crystal segment size was 1×1 mm^2 and the crystal thickness was 20 mm. The fill factor was 86.5%. The energy resolution, time resolution, and DOI resolution were assumed to be 15%, 400 ps, and 2 mm, respectively, [35]–[37]. The time window and energy window for selecting coincidence events were 1 ns and [400, 620] keV, respectively. For the CZT system, the crystal size was $40 \times 40 \times 5$ mm^3, and the energy resolution, time resolution, and intrinsic spatial resolution were set to 2%, 8 ns, and $1 \times 1 \times 1$ mm^3, respectively [19]. The time window was 15 ns and energy window was [490, 530] keV. The deadtime of the LYSO scanner and CZT scanner were set as 1 μs and 10 μs, based on PETsys TOFPET2 ASIC [38] and Kromek RENA3 ASIC [39], respectively.

The photon coincidence sensitivity was defined as the coincidence rate divided by the point source activity. Generally, only photons without scattering were used to constitute coincidences (P-P coincidence). To further improve sensitivity, MIPEs have been recovered with different methods [40]–[43]. In this article, Compton kinematics [40] was used to recover coincidences (P-CP coincidence) between annihilation photons that had a photoelectric event (P photon) and photons that had a Compton event before the photoelectric event (CP photon). In Compton kinematics, the scattering angle can be computed by energy

$$\theta_E = \cos^{-1}\left(1 - m_0c^2\left(\frac{1}{E_s} - \frac{1}{E_i}\right)\right) \tag{1}$$

where E_i is the incident photon energy, E_s is the scattered photon energy, and m_0c^2 is the rest mass of an electron. For PET applications, $E_i = m_0c^2 = 511$ keV. The scattering angle can also be computed using the interaction position information

$$\theta_p = \cos^{-1}\left(\frac{\vec{V_i} \cdot \vec{V_s}}{\left|\vec{V_i}\right| \cdot \left|\vec{V_s}\right|}\right) \tag{2}$$

where $\vec{V_i}$ and $\vec{V_s}$ are the directions of incident and scattered photons. Fig. 2 shows the principle to identify the Compton event in a P-CP coincidence. To compare the sensitivity and MIPE recoverability of the two systems and check the performance of Compton kinematics under a high single rate, 10 point sources with different activities (7, 14, . . . , 70 MBq) placed at the FOV center were simulated separately. Since the crystal size of many previously published dedicated brain PET scanners are around 2 mm [25], [27], [44]–[46], we compared the Compton recovery accuracy of systems based on 1-mm crystal size and 2-mm crystal size, respectively.

NEC rate incorporates the noise effects of random and scatter counts and is an indicator of the signal-to-noise ratio

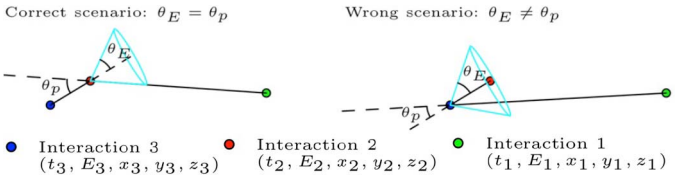

Fig. 2. Using Compton kinematics to identify the Compton event in a P-CP coincidence. The sequence with a smaller $|\theta_E - \theta_p|$ is picked up.

for the PET systems [47]

$$\text{NEC} = \frac{T^2}{T + S + R} \tag{3}$$

where T, S, and R are true, scatter, and random coincidence rates, respectively. To consider the effect of activity outside of the FOV, the phantom used for the NEC study contained three components, which represented the brain, neck, and torso. The brain component was a 130-mm diameter and 80-mm height cylinder with a 45.6 kBq/cm^3 concentration activity [48], and the torso component was a 260-mm diameter and 200-mm height cylinder with 5.7 kBq/cm^3. Both the brain and the torso were placed outside the FOV. For the neck component [14] (cylinder, 110-mm diameter, 126-mm height), ten different concentration activities (5.7, 11.4, . . . , 57 kBq/cm^3) were investigated.

For a stationary two-panel geometry, the incomplete angular sampling would cause the orthogonal-panel spatial resolution to be worse than the in-panel spatial resolution. To understand the difference, a point source was placed at the FOV center, and the line profiles along the orthogonal-panel and in-panel directions in the reconstructed image were fitted separately to measure the spatial resolution. Images were reconstructed with a list-mode 3-D maximum-likelihood expectation maximization (MLEM) algorithm [49] through the gpurecon program [50]. Time-of-flight (TOF) is known to have the large potential for image quality improvement and more accurate quantification (signal-to-noise ratio) for a given number of counts [51], [52], and TOF was incorporated in the image reconstruction of the LYSO system. As a comparison, the CZT system did not utilize TOF.

B. System Geometry

For the system geometry study, four CZT systems with two-panel, lengthened two-panel, four-panel, and full-ring geometries were compared, as shown in Fig. 3. All four systems have 150-mm thickness in the z-axis. The panel size of the two-panel and the four-panel systems was 40×200 mm^2, while the panel in the lengthened two-panel system was 40×320 mm^2. The average human head size was 145 mm (head breadth) $\times$ 194 mm (head thickness) in the United States, and the maximum head size was 174 mm $\times$ 239 mm [34]. Since the distance between detector panels was adjustable, the distance between panels was set as 24 cm based on the average human head size. On the contrary, the full-ring structure did not have the flexibility to adjust its geometry, so the inner diameter was set as 30 cm based on the maximum human head size. The time resolution and energy resolution were set as 8 ns and 2%,

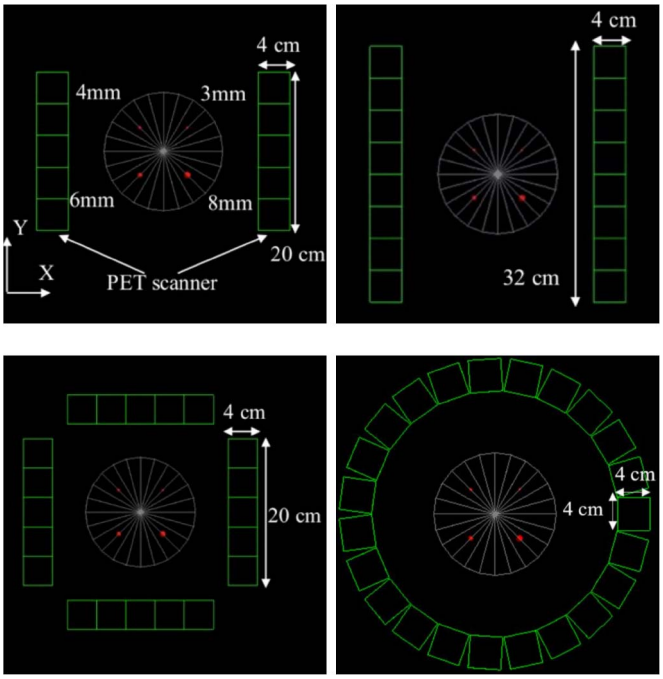

Fig. 3. Four CZT systems with two-panel (top-left), lengthened two-panel (top-right), four-panel (bottom-left), and full-ring (bottom-right) geometries were used for the phantom study. The x- and y-axes are shown in the figure, and the z-axis is perpendicular to the paper. All four systems have the same 150-mm thickness in the z-axis.

respectively. The time window was 15 ns and energy window was [490, 530] keV. P-CP coincidences were used in the image reconstruction.

For the cylinder phantom study, four hot spheres with diameters 3, 4, 6, and 8 mm were placed in a 126-mm height, 110-mm diameter water phantom. The background concentration activity was 5.7 kBq/cm^3, and the hot-to-background ratio was 8:1 [14]. We further compared the four geometries based on 1-mm crystal size and 2-mm crystal size. Each system had a 2-min data acquisition.

The same MLEM gpurecon program without TOF was used for image reconstruction. For the 1-mm crystal size, the voxel size of reconstructed image was $0.5 \times 0.5 \times 0.5$ mm^3. As a comparison, the voxel size of the 2-mm crystal size was $1 \times 1 \times 1$ mm^3. The image reconstruction had ten iterations, which was chosen to maximize the CNR of the 3-mm sphere in the cylinder phantom study. Data corrections for scatter coincidence and random coincidence were not applied. No regularization or a post-reconstruction filter was used.

Image quality was evaluated based on CRC and CNR [53]

$$\text{CRC} = \frac{C_{\text{hot}}/C_{bkg} - 1}{a_{\text{hot}}/a_{bkg} - 1}, \quad \text{CNR} = \frac{C_{\text{hot}} - C_{bkg}}{\sigma_{bkg}} \tag{4}$$

where C_{hot} and C_{bkg} are the average voxel value in a hot sphere and background region of interest (ROI), respectively, a_{hot} and a_{bkg} are the ground-truth concentration activity, and σ_{bkg} is the standard deviation of the voxel values in the background ROI.

For the XCAT phantom [54] study, simulations of the lengthened two-panel system and the four-panel system on the XCAT phantom in head and neck region

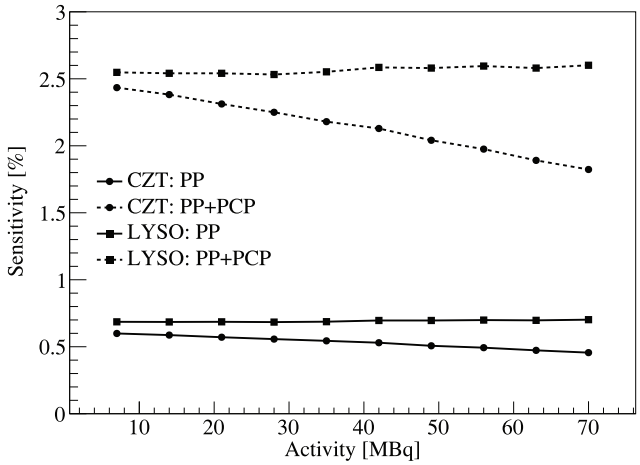

Fig. 4. Sensitivity w/o and w/ Compton recovery of the CZT and LYSO systems under different source activities. The crystal size of both system is 1 mm.

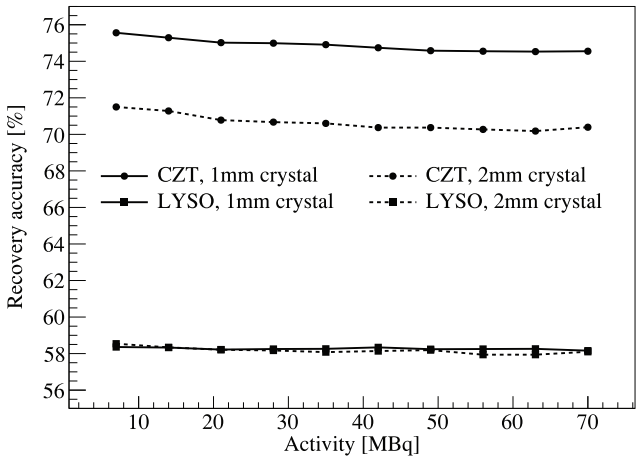

Fig. 5. Compton recovery accuracy of the CZT and LYSO systems based on 1-mm and 2-mm crystal size, respectively.

($200 \times 240 \times 150$ mm^3 in x-, y-, and z-axes) were performed. The ^{18}F-FDG concentration activity in normal tissue, spinal cord, salivary gland, and brain were 3.4, 7.1, 7.8, and 16.9 kBq/cm^3 based on clinical study, respectively [14], [48], [55], [56]. A sphere tumor with 5-mm diameter was put inside the phantom and the tumor concentration activity was 27.2 kBq/cm^3. Each system had a 6-min data acquisition [14].

C. Comparison With Whole-Body Scanner

To validate the benefits of the add-on dedicated system, another simulation was performed to compare the two-panel scanner with one whole-body PET scanner (GE Discovery MI 4-ring PET scanner). The same cylinder phantom (11-cm diameter and 12.6-cm length) were simulated with both systems, respectively. Hot spheres (nine 3-mm diameter, nine 4-mm diameter, five 6-mm diameter, and five 8-mm diameter) were placed in the central slice of the axial direction of the phantom. The background activity was 5700 Bq/cm^3, and the sphere to background ratio was 8:1.

III. Results

A. Detecting Material

The sensitivity of the CZT and LYSO systems under different source activities is shown in Fig. 4. At 7 MBq, the sensitivity of the CZT and LYSO systems are 0.60% and 0.69%, and it increased to 2.43% and 2.55%, respectively, after recovering MIPEs. The results showed that with a 40-mm crystal thickness, the CZT system could achieve similar sensitivity as the LYSO system. After recovering MIPEs, the sensitivity of both systems improved approximately 3 times, which indicated the importance of MIPE recovery. Due to the poor time resolution, the P-CP sensitivity of the CZT system decreased 25.5% with the increase of activity from 7 MBq to 70 MBq. This was because if more than two interactions were detected within the same time window, all the events within this time window were abandoned. So when the count rate got higher, it was more likely that more than two interactions were detected within the same time window, and lowered the sensitivity.

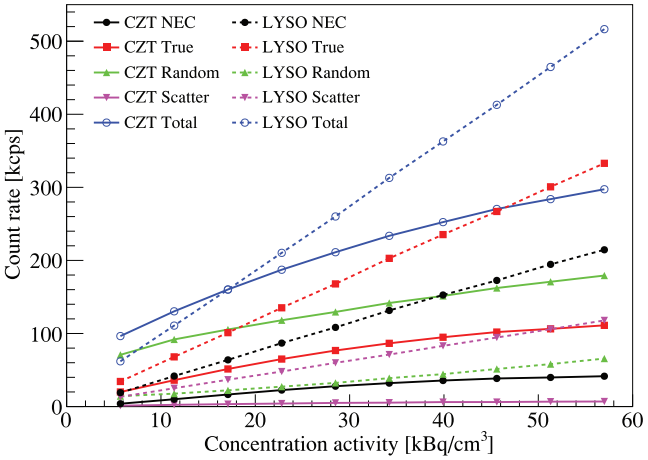

Fig. 6. NEC, true, random, scatter, and the total rate of the CZT and LYSO systems. The concentration activity only refers to the neck phantom, while that of the brain and the torso phantoms are kept as the same during the sweeping.

The P-CP coincidences recovery accuracy of the CZT and LYSO systems based on 1-mm and 2-mm crystal is shown in Fig. 5. The results also showed that given a source activity, the recovery accuracy of the CZT system was about 20% higher than LYSO, and the recovery accuracy was not affected by the source activity. By decreasing the crystal size from 2 mm to 1 mm, the Compton recovery accuracy of the CZT system improved 4.23%, while that of the LYSO system was almost the same. This was because the Compton recovery accuracy was affected by both energy resolution and crystal size. For the CZT system, the energy resolution was high, so decreasing crystal size could improve accuracy. However, in the LYSO system, the poor energy resolution dominated the recovery error, so changing crystal size did not make an obvious influence. Details can be found in our previous study [57].

The NEC, true, random, scatter, and the total rate of the CZT and LYSO systems are shown in Fig. 6. The LYSO system

TABLE I
POINT SOURCE SPATIAL RESOLUTION OF THE CZT AND LYSO SYSTEM

spatial resolution	P-P coincidences	P-P and P-CP coincidences
CZT in-panel	0.56 mm	0.58 mm
CZT orthogonal-panel	0.71 mm	0.74 mm
LYSO in-panel	0.62 mm	0.70 mm
LYSO orthogonal-panel	1.31 mm	1.40 mm

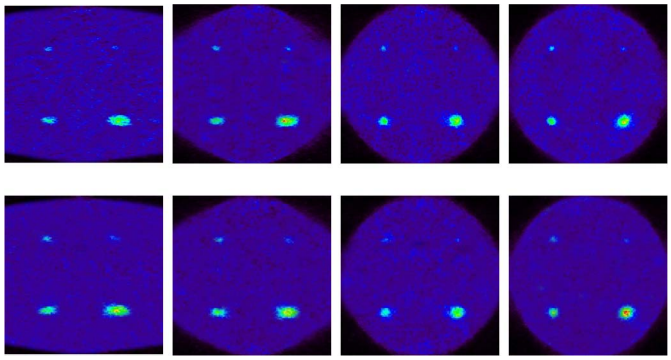

Fig. 7. Reconstructed images of the cylinder phantom with hot spheres. The top row is the results based on 1-mm crystal size, and the voxel size of the reconstructed image is $0.5 \times 0.5 \times 0.5$ mm^3. The bottom row is the results based on 2-mm crystal size, and the voxel size is $1 \times 1 \times 1$ mm^3. From left to right, the four systems are two-panel, lengthened two-panel, four-panel, and full-ring, respectively.

showed a high NEC rate at all concentration activities, and the higher the concentration activity, the larger the difference was.

The in-panel and orthogonal-panel spatial resolution of CZT and LYSO systems based on only P-P coincidences and both P-P and P-CP coincidences are shown in Table I. The results indicated that CZT had a better spatial resolution than LYSO, and incorporating P-CP coincidences for image reconstruction would slightly deteriorate the spatial resolution.

B. System Geometry

The reconstructed images of the cylinder phantom are shown in Fig. 7. The 4-, 6-, and 8-mm hot spheres were clearly resolvable in all four systems. Due to the limited angular data sampling, the background and hot spheres were elongated in the two-panel and lengthened two-panel systems. CRC and CNR versus hot sphere diameters curves are shown in Fig. 8.

The reconstructed images of the XCAT phantom are shown in Fig. 9. The spinal cord, salivary gland, and brain were clearly resolvable in both images. The tumor was also visible in both systems within 6 min, but the tumor in the four-panel system was more resolvable. The tumor CRC were 0.08 and 0.12 for the lengthened two-panel system and the four-panel system, respectively, while the CNR of the tumor were 2.4 and 4.2.

C. Comparison With Whole-Body Scanner

The transverse slices and the sagittal slice reconstructed images of the dedicated two-panel scanner and the dedicated scanner are shown in Fig. 10. It can be shown that the dedicated system can achieve superior spatial resolution than the whole body system, which indicates the benefits of using such an add-on system.

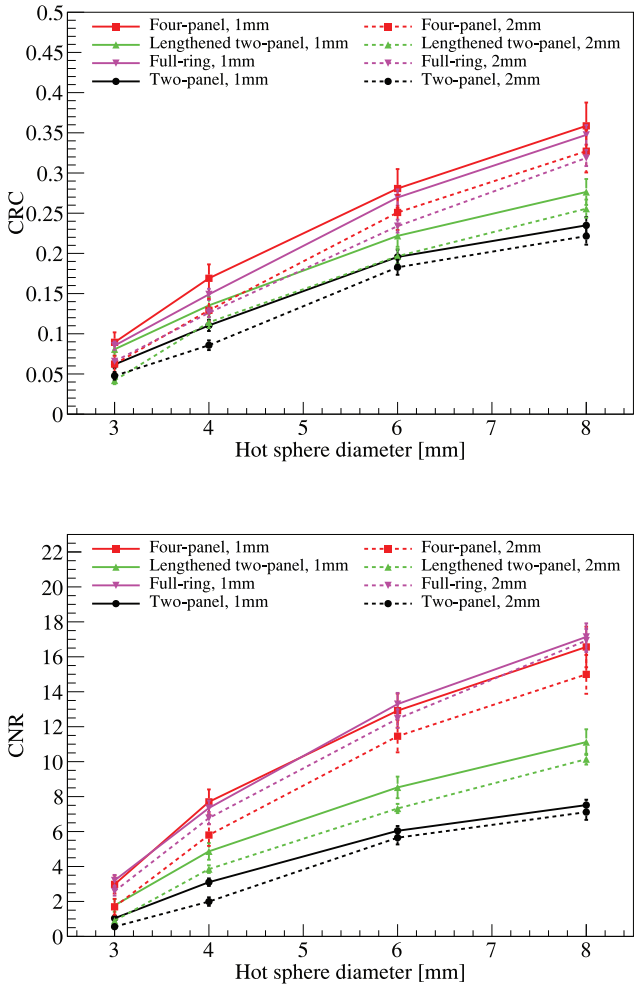

Fig. 8. CRC (top) and CNR (bottom) versus hot sphere diameter for different system geometries and different crystal size.

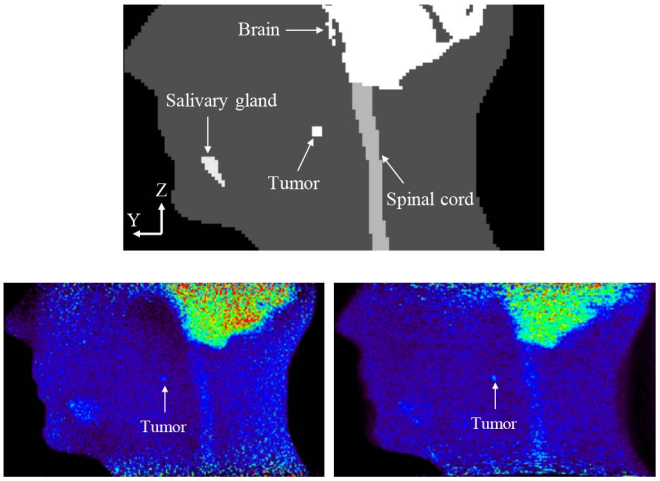

Fig. 9. Reconstructed images of the XCAT phantom in head and neck region. Top: concentration activity map. Bottom left: the lengthened two-panel system. Bottom right: the four-panel system.

IV. DISCUSSION

We studied the design considerations for a dedicated HNC PET scanner. Different detecting material, including CZT and LYSO, and different system geometries, including two-panel,

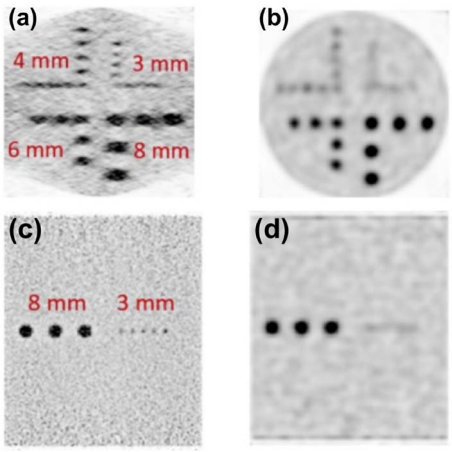

Fig. 10. Comparison of the two-panel dedicated system and a whole-body scanner (GE Discovery MI 4-ring PET scanner). (a) Transverse slice of the dedicated scanner. (b) Transverse slice of the whole body scanner. (c) Sagittal slice of the dedicated scanner. (d) Sagittal slice of the whole body scanner.

lengthened two-panel, four-panel, and full-ring geometries, were investigated.

A. Detecting Material

For the detecting material, CZT and LYSO were compared in terms of sensitivity, MIPEs recovery, NEC rate, and spatial resolution. The sensitivity of CZT was 13.04% lower than the LYSO, which suggests that the CZT system and the LYSO system with exactly the same geometry can achieve comparable sensitivity. After recovering MIPEs, the sensitivity of CZT was only 4.71% lower, which indicates that the CZT could recover more MIPEs than LYSO. This is because CZT has a larger Compton-to-photoelectric ratio than the LYSO. Moreover, due to the much better energy resolution, CZT showed about 20% higher recovery accuracy. The large Compton-to-photoelectric ratio and the high energy resolution make CZT better for the MIPEs recovery.

Though the LYSO system had a larger scatter event rate, it showed a high NEC rate due to its larger true event rate and smaller random event rate. In the data processing, if photons from more than one annihilation were detected in a time window, all singles in this window were rejected. When the total activity was high, the probability to detect more annihilation photons within one window got increased. Since CZT had a wide time window (15 ns), the true coincidence rate of CZT gradually plateaued. The poor time resolution also led to a much higher random rate for the CZT system compared to the LYSO system. The low true rate and high random rate caused the NEC rate for the CZT system to be lower than that of the LYSO system. A lead shield for stopping singles from outside of the FOV is likely necessary for the CZT system.

Table I shows that the in-panel and orthogonal-panel spatial resolution of the CZT decreased 3.57% and 4.23% after incorporating P-CP coincidences. As a comparison, the LYSO system decreased by 12.90% and 6.87%, respectively. The spatial resolution gets worse because incorrectly recovered P-CP coincidences were used for image reconstruction. However, since LYSO has a worse recovery accuracy, the deterioration of spatial resolution is worse than CZT.

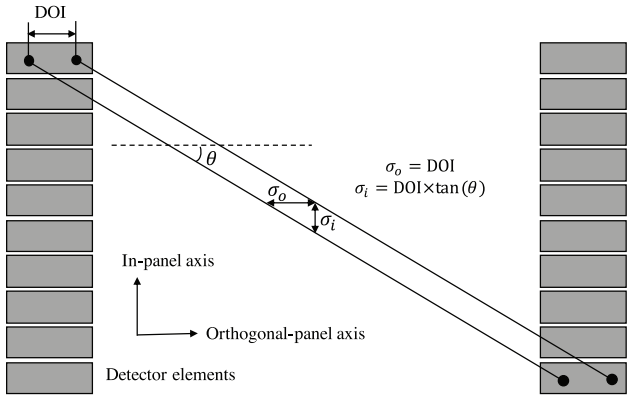

Fig. 11. Illustration of how DOI affects the in-panel and orthogonal-panel spatial resolution in a stationary two-panel geometry PET system.

Table I also shows that the CZT system has a better in-panel and orthogonal-panel spatial resolution than LYSO. For a stationary two-panel geometry, DOI affects both the in-panel and orthogonal-panel spatial resolution [18], which is illustrated in Fig. 11. For the sake of simplicity, a 2-D case is drawn. The spatial resolution is limited by the closest distinguishable LORs. For two adjacent LORs, the blurring along the orthogonal-panel axis σ_o is equal to DOI, while the blurring along the in-panel axis σ_i is equal to DOI $\times \tan(\theta)$, where θ is the angle between the LOR and the orthogonal-panel axis. In a stationary two-panel geometry system, the LOR with a small θ has a large probability to be detected. As a result, σ_o tends to be larger than σ_i, which explains why the orthogonal-panel spatial resolution is worse than the in-panel spatial resolution. The result shows the importance of DOI resolution to a two-panel geometry system.

B. System Geometry

For the system geometry, four CZT systems with two-panel, lengthened two-panel, four-panel, and full-ring geometries were compared in terms of CRC and CNR of the reconstructed image. For all four scanners, both CRC and CNR improved with increasing sphere diameter, and the difference in CRC and CNR among all scanners increased as the diameter of the sphere increased. For all four geometries, the CRC and CNR of 1-mm crystal size were higher than the 2-mm crystal size, which indicated the benefits of using 1-mm crystal.

Compared with the two-panel scanner, the lengthened two-panel scanner had a higher CRC and CNR in 4-, 6- and 8-mm spheres. Compared with the two limited-angle (two-panel, lengthened two-panel) scanners, the two full-geometry (four-panel, full-ring) scanners could achieve higher CRC and CNR in all spheres. However, the improvement of CRC and CNR comes with the need for more detectors. Specifically, the ratio of the number of detectors of the two-panel, lengthened two-panel, four-panel, and full-ring geometries are 10:16:20:23, which means that the full-geometry (four-panel, full-ring) designs achieve higher CRC and CNR in large lesions with a doubled cost, due to the doubled number of detectors.

Moreover, panel-based designs have the flexibility to adjust the panel distance while the same image reconstruction method can still be used, so that the system geometry is able to be compactly adapted to individual patients. It is also very important to consider the patient's comfort in such a compact design, and two-panel can achieve this goal without blocking the line of sight.

C. Comparison With Virtual-Pinhole PET

Virtual-pinhole PET is known as using a high-resolution add-on PET scanner to improve the spatial resolution. Depends on different regions of interest, virtual-pinhole PET can have different geometries (full-ring for small animal imaging [58], half-ring for head and neck imaging [59] and breast imaging [60]). The idea of the virtual-pinhole PET and the dedicated PET proposed in this article are similar, both of which use smaller crystals and are placed near the ROI to improve the spatial resolution locally.

However, the main difference is that the virtual-pinhole PET is inserted into the whole-body PET and it acquires data with the whole-body PET simultaneously (a task that is not trivial and requires working with whole-body vendors), thus there are three types of coincidence events: insert–insert, insert–scanner, and scanner–scanner [61]. As a result, the insertion of the virtual-pinhole PET affects the photon detection of the whole-body PET and image reconstruction is more complex because two systems need to be modeled at the same time. As a comparison, the dedicated PET acquires data with whole-body PET separately, so photon detection of the whole-body PET is not affected. However, since we want to use the whole-body PET image as the prior image to reduce the limited artifacts in the dedicated PET image, it is necessary to track patient movement for the dedicated PET application, which brings extra complexity.

D. Limited-Angle Artifacts

The stationary two-panel PET system is known to have the limited-angle artifacts [62]–[66]. Fig. 7 shows that both the two-panel and lengthened two-panel systems have an elongated background and hot spheres. One method to reduce the limited-angle artifacts is to use a prior image without limited angle artifacts and penalize the dissimilarity between the target image and the prior image during the reconstruction [67], [68]. We plan to take advantage of a whole-body PET scan, which does not have the problem of limited-angle artifacts and the whole-body PET image can be used as the prior image. We are developing the penalized maximum-likelihood image reconstruction algorithm.

V. Conclusion

In this article, we evaluated different detecting materials and system geometries through the simulation of a dedicated HNC PET scanner. For comparing the detecting material, the sensitivity of the 40-mm thickness CZT system and the 20-mm LYSO system are 0.60% and 0.69%, and it increases to 2.43% and 2.55%, respectively, after recovering MIPEs. The favorable energy resolution makes the CZT system have an approximately 20% higher MIPE recovery accuracy, but the poor time resolution of CZT results in a two-times lower NEC rate. However, the superior DOI resolution of CZT leads to a better spatial resolution, which is important for HNC imaging. For comparing system geometry, the four-panel and full-ring PET systems achieve higher CRC and CNR than the two-panel and lengthened two-panel PET systems. Nevertheless, the CRC of the 3-mm diameter hot sphere of the two-panel and lengthened two-panel PET systems is comparable to that of the four-panel and full-ring PET systems. The CRC and CNR for the two-panel system can be improved by extending the panel size. Both the two-panel and four-panel PET systems can image the patient's head and neck region and resolve a 5-mm lesion within 6 min. The disadvantage of the four-panel and full-ring PET systems is that they are in the line of sight of the patient, which compromises the patient's comfort. To summarize, the CZT system can achieve better spatial resolution and recovery accuracy of MIPEs compared to the LYSO system. However, the poor timing resolution of the CZT system yields a lower sensitivity, especially at high source activity. For system geometry, full-ring and four-panel designs have better CRC and CNR than two-panel design, but they come with a higher cost and compromised patient's comfort.

Acknowledgment

The authors would also like to thank the Molecular Imaging Instrumentation Laboratory at Stanford University for help with the gpurecon program.

References

[1] R. L. Siegel, K. D. Miller, and A. Jemal, "Cancer statistics, 2017," *Cancer J. Clin.*, vol. 67, no. 1, pp. 7–30, 2017.

[2] R. Subramaniam, M. Truong, P. Peller, O. Sakai, and G. Mercier, "Fluorodeoxyglucose–positron–emission tomography imaging of head and neck squamous cell cancer," *Amer. J. Neuroradiol.*, vol. 31, no. 4, pp. 598–604, 2010.

[3] B. Nowak *et al.*, "Diagnostic evaluation of malignant head and neck cancer by F-18-FDG PET compared to CT/MRI," *Nuklearmedizin Archive*, vol. 38, no. 8, pp. 312–318, 1999.

[4] D. L. Schwartz *et al.*, "FDG-PET/CT imaging for preradiotherapy staging of head-and-neck squamous cell carcinoma," *Int. J. Radiat. Oncol. Biol. Phys.*, vol. 61, no. 1, pp. 129–136, 2005.

[5] S.-M. Eschmann *et al.*, "Prognostic impact of hypoxia imaging with 18F-misonidazole PET in non-small cell lung cancer and head and neck cancer before radiotherapy," *J. Nucl. Med.*, vol. 46, no. 2, pp. 253–260, 2005.

[6] M. Majdoub *et al.*, "Prognostic value of head and neck tumor proliferative sphericity from 3-Deoxy–[18F] fluorothymidine positron emission tomography," *IEEE Trans. Radiat. Plasma Med. Sci.*, vol. 2, no. 1, pp. 33–40, Jan. 2018.

[7] S. Adams, R. P. Baum, T. Stuckensen, K. Bitter, and G. Hör, "Prospective comparison of 18F-FDG PET with conventional imaging modalities (CT, MRI, U.S.) in lymph node staging of head and neck cancer," *Eur. J. Nucl. Med. Mol. Imag.*, vol. 25, no. 9, pp. 1255–1260, 1998.

[8] M. N. Lonsdale and T. Beyer, "Dual-modality PET/CT instrumentation—Today and tomorrow," *Eur. J. Radiol.*, vol. 73, no. 3, pp. 452–460, 2010.

[9] R. Yao, R. Lecomte, and E. S. Crawford, "Small-animal PET: What is it, and why do we need it?" *J. Nucl. Med. Technol.*, vol. 40, no. 3, pp. 157–165, 2012.

[10] E. J. Hoffman, S.-C. Huang, and M. E. Phelps, "Quantitation in positron emission computed tomography: 1. Effect of object size." *J. Comput. Assist. Tomography*, vol. 3, no. 3, pp. 299–308, 1979.

[11] F. Hofheinz *et al.*, "Increased evidence for the prognostic value of primary tumor asphericity in pretherapeutic FDG PET for risk stratification in patients with head and neck cancer," *Eur. J. Nucl. Med. Mol. Imag.*, vol. 42, no. 3, pp. 429–437, 2015.

[12] Y. Yamazaki *et al.*, "Assessment of cervical lymph node metastases using FDG-PET in patients with head and neck cancer," *Ann. Nucl. Med.*, vol. 22, no. 3, pp. 177–184, 2008.

[13] R. S. Rodrigues *et al.*, "Comparison of whole-body PET/CT, dedicated high-resolution head and neck PET/CT, and contrast-enhanced CT in preoperative staging of clinically M0 squamous cell carcinoma of the head and neck," *J. Nucl. Med.*, vol. 50, no. 8, pp. 1205–1213, 2009.

[14] Y. Yamamoto, T. Z. Wong, T. G. Turkington, T. C. Hawk, and R. E. Coleman, "Head and neck cancer: Dedicated FDG PET/CT protocol for detection-phantom and initial clinical studies," *Radiology*, vol. 244, no. 1, pp. 263–272, 2007.

[15] A. Argiris, M. V. Karamouzis, D. Raben, and R. L. Ferris, "Head and neck cancer," *Lancet*, vol. 371, no. 9625, pp. 1695–1709, 2008.

[16] R. E. Carson and P. H. Kuo, "Brain-dedicated emission tomography systems: A perspective on requirements for clinical research and clinical needs in brain imaging," *IEEE Trans. Radiat. Plasma Med. Sci.*, vol. 3, no. 3, pp. 254–261, May 2019.

[17] B. F. Hutton, T. Yamaya, and L. R. Furenlid, "Dedicated molecular imaging systems for human neurological studies," *IEEE Trans. Radiat. Plasma Med. Sci.*, vol. 3, no. 3, pp. 252–253, May 2019.

[18] H. Peng and C. S. Levin, "Design study of a high-resolution breast-dedicated PET system built from cadmium zinc telluride detectors," *Phys. Med. Biol.*, vol. 55, no. 9, p. 2761, 2010.

[19] S. Abbaszadeh, Y. Gu, P. D. Reynolds, and C. S. Levin, "Characterization of a sub-assembly of 3D position sensitive cadmium zinc telluride detectors and electronics from a sub-millimeter resolution pet system," *Phys. Med. Biol.*, vol. 61, no. 18, p. 6733, 2016.

[20] A. Drezet, O. Monnet, F. Mathy, G. Montemont, and L. Verger, "CdZnTe detectors for small field of view positron emission tomographic imaging," *Nucl. Instrum. Methods Phys. Res. A Accelerators Spectrometers Detectors Assoc. Equip.*, vol. 571, nos. 1–2, pp. 465–470, 2007.

[21] P. Vaska *et al.*, "A prototype CZT-based PET scanner for high resolution mouse brain imaging," in *Proc. IEEE Nucl. Sci. Symp. Conf. Rec. (NSS)*, vol. 5, 2007, pp. 3816–3819.

[22] G. S. Mitchell *et al.*, "CdTe strip detector characterization for high resolution small animal PET," *IEEE Trans. Nucl. Sci.*, vol. 55, no. 3, pp. 870–876, Jun. 2008.

[23] Y. Morimoto *et al.*, "Development of a 3D brain PET scanner using CdTe semiconductor detectors and its first clinical application," *IEEE Trans. Nucl. Sci.*, vol. 58, no. 5, pp. 2181–2189, Oct. 2011.

[24] A. J. González, F. Sánchez, and J. M. Benlloch, "Organ-dedicated molecular imaging systems," *IEEE Trans. Radiat. Plasma Med. Sci.*, vol. 2, no. 5, pp. 388–403, Sep. 2018.

[25] C. E. Bauer *et al.*, "Concept of an upright wearable positron emission tomography imager in humans," *Brain Behav.*, vol. 6, no. 9, 2016, Art. no. e00530.

[26] S. Yamamoto, M. Honda, T. Oohashi, K. Shimizu, and M. Senda, "Development of a brain PET system, PET-Hat: A wearable PET system for brain research," *IEEE Trans. Nucl. Sci.*, vol. 58, no. 3, pp. 668–673, Jun. 2011.

[27] H. Tashima *et al.*, "Development of the helmet-chin PET prototype," in *Proc. IEEE Nucl. Sci. Symp. Med. Imag. Conf. (NSS/MIC)*, 2015, pp. 1–3.

[28] H. W. De Jong, F. H. Van Velden, R. W. Kloet, F. L. Buijs, R. Boellaard, and A. A. Lammertsma, "Performance evaluation of the ECAT HRRT: An LSO-LYSO double layer high resolution, high sensitivity scanner," *Phys. Med. Biol.*, vol. 52, no. 5, pp. 1505–1526, 2007.

[29] L. MacDonald, J. Edwards, T. Lewellen, D. Haseley, J. Rogers, and P. Kinahan, "Clinical imaging characteristics of the positron emission mammography camera: PEM flex solo II," *J. Nucl. Med.*, vol. 50, no. 10, pp. 1666–1675, 2009.

[30] A. Ferrero, Q. Peng, G. W. Burkett, Jr., B. Sumanasena, W. W. Moses, and R. D. Badawi, "Preliminary performance characterization of DbPET2.1, a PET scanner dedicated to the imaging of the breast and extremities," *Biomed. Phys. Eng. Exp.*, vol. 1, no. 1, 2015, Art. no. 015202.

[31] K. K. Miyake *et al.*, "Performance evaluation of a new dedicated breast PET scanner using NEMA NU4-2008 standards," *J. Nucl. Med.*, vol. 55, no. 7, pp. 1198–1203, 2014.

[32] L. Moliner *et al.*, "Design and evaluation of the MAMMI dedicated breast PET," *Med. Phys.*, vol. 39, no. 9, pp. 5393–5404, 2012.

[33] S. Jan *et al.*, "GATE: A simulation toolkit for PET and SPECT," *Phys. Med. Biol.*, vol. 49, no. 19, pp. 4543–4561, 2004.

[34] J.-H. Lee, S. Hwang, and C. L. Istook, "Analysis of human head shapes in the United States," *Int. J. Human Ecol.*, vol. 7, no. 1, pp. 77–83, 2006.

[35] G. Sportelli *et al.*, "The TRIMAGE PET data acquisition system: Initial results," *IEEE Trans. Radiat. Plasma Med. Sci.*, vol. 1, no. 2, pp. 168–177, Mar. 2017.

[36] S. Majewski *et al.*, "HelmetPET: A silicon photomultiplier based wearable brain imager," in *Proc. IEEE Nucl. Sci. Symp. Med. Imag. Conf. (NSS/MIC)*, 2011, pp. 4030–4034.

[37] M. Li and S. Abbaszadeh, "Depth-of-interaction study of a dual-readout detector based on TOFPET2 application-specific integrated circuit," *Phys. Med. Biol.*, vol. 64, no. 17, 2019, Art. no. 175008.

[38] A. Di Francesco *et al.*, "TOFPET2: A high-performance ASIC for time and amplitude measurements of SiPM signals in time-of-flight applications," *J. Instrum.*, vol. 11, no. 3, 2016, Art. no. C03042.

[39] V. B. Cajipe *et al.*, "Performance of the RENA-3 IC with position-sensitive CZT and CdTe detectors," in *Proc. IEEE Nucl. Sci. Symp. Conf. Rec.*, 2008, pp. 300–307.

[40] S. Abbaszadeh, G. Chinn, and C. S. Levin, "Positioning true coincidences that undergo inter-and intra-crystal scatter for a sub-mm resolution cadmium zinc telluride-based PET system," *Phys. Med. Biol.*, vol. 63, no. 2, 2018, Art. no. 025012.

[41] J. E. Gillam *et al.*, "Sensitivity recovery for the AX-PET prototype using inter-crystal scattering events," *Phys. Med. Biol.*, vol. 59, no. 15, pp. 4065–4083, 2014.

[42] A. A. Wagadarikar, A. Ivan, S. Dolinsky, and D. L. McDaniel, "Sensitivity improvement of time-of-flight (TOF)-PET detector through recovery of Compton scattered annihilation photons," in *Proc. IEEE Nucl. Sci. Symp. Med. Imag. Conf. (NSS/MIC)*, 2012, pp. 3178–3183.

[43] E. Yoshida, H. Tashima, and T. Yamaya, "Sensitivity booster for DOI-PET scanner by utilizing Compton scattering events between detector blocks," *Nucl. Instrum. Methods Phys. Res. A Accelerators Spectrometers Detectors Assoc. Equip.*, vol. 763, pp. 502–509, Nov. 2014.

[44] E. Yoshida *et al.*, "The jPET-D4: Performance evaluation of four-layer DOI-PET scanner using the NEMA NU2-2001 standard," in *Proc. IEEE Nucl. Sci. Symp. Conf. Rec.*, vol. 4, 2006, pp. 2532–2536.

[45] K. Wienhard *et al.*, "The ECAT HRRT: Performance and first clinical application of the new high resolution research tomograph," *IEEE Trans. Nucl. Sci.*, vol. 49, no. 1, pp. 104–110, Feb. 2002.

[46] K. Gong *et al.*, "Designing a compact high performance brain PET scanner-simulation study," *Phys. Med. Biol.*, vol. 61, no. 10, pp. 3681–3697, 2016.

[47] S. C. Strother, M. E. Casey, and E. J. Hoffman, "Measuring PET scanner sensitivity: Relating countrates to image signal-to-noise ratios using noise equivalents counts," *IEEE Trans. Nucl. Sci.*, vol. 37, no. 2, pp. 783–788, Apr. 1990.

[48] H. Engel, H. Steinert, A. Buck, T. Berthold, R. A. H. Böni, and G. K. von Schulthess, "Whole-body PET: Physiological and artifactual fluorodeoxyglucose accumulations," *J. Nucl. Med.*, vol. 37, no. 3, pp. 441–445, 1996.

[49] L. A. Shepp and Y. Vardi, "Maximum likelihood reconstruction for emission tomography," *IEEE Trans. Med. Imag.*, vol. MI-1, no. 2, pp. 113–122, Oct. 1982.

[50] J. Cui, G. Pratx, B. Meng, and C. S. Levin, "Distributed MLEM: An iterative tomographic image reconstruction algorithm for distributed memory architectures," *IEEE Trans. Med. Imag.*, vol. 32, no. 5, pp. 957–967, May 2013.

[51] S. Vandenberghe, E. Mikhaylova, E. D'Hoe, P. Mollet, and J. S. Karp, "Recent developments in time-of-flight PET," *EJNMMI Phys.*, vol. 3, no. 1, p. 3, 2016.

[52] S. Surti and J. S. Karp, "Advances in time-of-flight PET," *Physica Medica*, vol. 32, no. 1, pp. 12–22, 2016.

[53] S. Surti and J. S. Karp, "Design considerations for a limited angle, dedicated breast, TOF PET scanner," *Phys. Med. Biol.*, vol. 53, no. 11, pp. 2911–2921, 2008.

[54] W. P. Segars, G. Sturgeon, S. Mendonca, J. Grimes, and B. M. W. Tsui, "4D XCAT phantom for multimodality imaging research," *Med. Phys.*, vol. 37, no. 9, pp. 4902–4915, 2010.

[55] Y. Nakamoto, M. Tatsumi, D. Hammoud, C. Cohade, M. M. Osman, and R. L. Wahl, "Normal FDG distribution patterns in the head and neck: PET/CT evaluation," *Radiology*, vol. 234, no. 3, pp. 879–885, 2005.

[56] K. A. Higgins *et al.*, "Analysis of pretreatment FDG-PET SUV parameters in head-and-neck cancer: Tumor SUVmean has superior prognostic value," *Int. J. Radiat. Oncol. Biol. Phys.*, vol. 82, no. 2, pp. 548–553, 2012.

[57] S. Yang, M. Li, M. Reed, J. Hugg, H. Chen, and S. Abbaszadeh, "Effect of CZT system characteristics on Compton scatter event recovery," *IEEE Trans. Radiat. Plasma Med. Sci.*, vol. 4, no. 1, pp. 91–97, Jan. 2020.

[58] H. Wu, D. Pal, T. Y. Song, J. A. O'Sullivan, and Y.-C. Tai, "Micro insert: A prototype full-ring PET device for improving the image resolution of a small-animal PET scanner," *J. Nucl. Med.*, vol. 49, no. 10, pp. 1668–1676, 2008.

[59] H. Wu *et al.*, "A high resolution PET insert system for clinical PET/CT scanners," in *Proc. IEEE Nucl. Sci. Symp. Conf. Rec.*, 2008, pp. 5442–5444.

[60] A. J. Mathews, S. Komarov, H. Wu, J. A. O'Sullivan, and Y.-C. Tai, "Improving PET imaging for breast cancer using virtual pinhole PET half-ring insert," *Phys. Med. Biol.*, vol. 58, no. 18, pp. 6407–6427, 2013.

[61] D. B. Keesing *et al.*, "Image reconstruction and system modeling techniques for virtual-pinhole PET insert systems," *Phys. Med. Biol.*, vol. 57, no. 9, p. 2517, 2012.

[62] E. Lee, M. E. Werner, J. S. Karp, and S. Surti, "Design optimization of a time-of-flight, breast PET scanner," *IEEE Trans. Nucl. Sci.*, vol. 60, no. 3, pp. 1645–1652, Jun. 2013.

[63] N. K. Doshi, R. W. Silverman, Y. Shao, and S. R. Cherry, "maxPET, a dedicated mammary and axillary region PET imaging system for breast cancer," *IEEE Trans. Nucl. Sci.*, vol. 48, no. 3, pp. 811–815, Jun. 2001.

[64] R. R. Raylman *et al.*, "The positron emission mammography/tomography breast imaging and biopsy system (PEM/PET): Design, construction and phantom-based measurements," *Phys. Med. Biol.*, vol. 53, no. 3, p. 637, 2008.

[65] M. F. Smith, R. R. Raylman, S. Majewski, and A. G. Weisenberger, "Positron emission mammography with tomographic acquisition using dual planar detectors: Initial evaluations," *Phys. Med. Biol.*, vol. 49, no. 11, pp. 2437–2452, 2004.

[66] M. C. Abreu *et al.*, "Design and evaluation of the clear-PEM scanner for positron emission mammography," *IEEE Trans. Nucl. Sci.*, vol. 53, no. 1, pp. 71–77, Feb. 2006.

[67] G.-H. Chen, J. Tang, and S. Leng, "Prior image constrained compressed sensing (PICCS): A method to accurately reconstruct dynamic CT images from highly undersampled projection data sets," *Med. Phys.*, vol. 35, no. 2, pp. 660–663, 2008.

[68] G.-H. Chen and Y. Li, "Synchronized multiartifact reduction with tomographic reconstruction (SMART-RECON): A statistical model based iterative image reconstruction method to eliminate limited-view artifacts and to mitigate the temporal-average artifacts in time-resolved CT," *Med. Phys.*, vol. 42, no. 8, pp. 4698–4707, 2015.